Defect Engineering in Semiconducting Oxides: Control of ZnO Surface Potential via Temperature and Oxygen Pressure

Ming Li and Edmund G. Seebauer
Dept. of Chemical and Biomolecular Engineering, University of Illinois, Urbana, IL 61801

DOI 10.1002/aic.15031
Published online September 21, 2015 in Wiley Online Library (wileyonlinelibrary.com)

The technological usefulness of a semiconductor often depends on the types, concentrations, charges, spatial distributions, and mobilities of the atomic-scale defects it contains. For semiconducting metal oxides, defect engineering is relatively new and involves complex transport and reaction networks. Surface-based methods hold special promise in nanostructures where surface-to-volume ratios are high. This work uses photoreflectance augmented by X-ray photoelectron spectroscopy to show that the surface potential V_S for Zn-terminated ZnO(0001) can be manipulated over a significant range 54.97–79.08 kJ/mol (0.57–0.82 eV) via temperature and the partial pressure of O_2. A defect transport model implies this variation in V_S should affect the injection rate of oxygen interstitials by a factor of three. Such injection plays an important role in controlling the concentrations of oxygen vacancies deep in the bulk, which often prove troublesome as trapping centers in photocatalysis and photovoltaics and as parasitic emitters in light-emitting devices.
 AIChE J, 62: 500–507, 2016
Keywords: defect engineering, metal oxide semiconductor, ZnO, photoreflectance spectroscopy

Introduction

In semiconductors, atomic-scale native defects such as vacancies and interstitial atoms affect the performance of microelectronic devices,[1] sensors,[2–4] catalysts,[5–7] photocatalysts,[8] photo-active devices,[9–11] and photovoltaic cells.[12] Accordingly, considerable effort has been expended in recent years to manipulate the type, concentration, spatial distribution, and mobility of such species—an endeavor termed "defect engineering." Examples of longstanding methods[13–17] include specially designed heating protocols (time, maximum temperature, heating, and cooling rates), introduction of foreign atoms, ion bombardment protocols, and amorphization/recrystallization. These approaches focus mostly on applications in Si-based microelectronics, with numerous reviews available.[13–18] Use of defect engineering outside of Si-based microelectronics is less extensive, with applications mainly for ion implantation in III–V compound semiconductors for devices[19–21] or metal oxide nanoparticles for photocatalysts.[22,23] For metal oxides in particular, the notion of defect engineering apart from ion implantation is relatively new, and only a few reviews can be found.[18,24,25] Noteworthy for the discipline of chemical engineering, recognition is taking root in the defect engineering community that complex transport and reaction networks characterize defect behavior in most prospective applications, and systems-based methods for parameter estimation in computational simulators are likely to play an important role in optimizing such networks.

Correspondence concerning this article should be addressed to E. G. Seebauer at eseebaue@uiuc.edu.

Existing methods for controlling defect behavior often suffer from problems with solid consumption, implantation damage, and foreign atom incorporation.[26] To mitigate these issues, this laboratory has proposed milder surface-based methods for both elemental and oxide semiconductors, including surface photostimulation[27,28] and manipulation of surface dangling bonds.[29,30] Surface-based methods hold special promise for defect manipulation in nanostructures where surface-to-volume ratios are high.

Along these lines, electric fields associated with built-in surface charge have been recently reported by this laboratory to influence the spatial distribution of native defects in oxide semiconductors such as TiO_2[31] by inducing a field-induced drift component to the transport. However, useful manipulation requires easy-to-implement mechanisms to control the electric field and the associated built-in potential that helps to control it. Moreover, development of computational tools for modeling the transport-reaction network[32] requires knowledge of the built-in potential. This work employs the *in situ* optical technique of photoreflectance (PR), augmented by a new data analysis method and X-ray photoelectron spectroscopy (XPS), to demonstrate two such mechanisms for Zn-terminated polar ZnO(0001): substrate temperature and gaseous oxygen adsorption. These two independently variable quantities permit reversible adjustment of the surface potential over a range that a defect transport model[31] implies should affect the injection rate of oxygen interstitials by a factor of three. Such injection plays an important role in controlling the concentrations of oxygen vacancies deep in the bulk, which often prove troublesome as trapping centers in photocatalysis and photovoltaics[33] and as parasitic emitters in light-emitting devices.[34,35]

Experiment

PR is a contactless optical modulation spectroscopy[28] in which the built-in surface electric field of a semiconductor is periodically perturbed by photocarriers generated via illumination with light having a photon energy greater than the fundamental band gap E_g. Photogenerated minority carriers migrate to the surface and neutralize a portion of any excess charge residing there. The consequent change in built-in surface electric field perturbs the reflectance R in narrow regions of wavelength corresponding to critical points in the band structure of the semiconductor. The small reflectance change ΔR is monitored with phase sensitive detection as a function of the photon energy E. Non-zero values for ΔR somewhere in the spectrum of $\Delta R/R$ vs. E conclusively manifest the existence of surface band bending. Coupling with an anchor bending value and direction measurement by XPS, PR scans as a function of temperature T, and perturbing beam intensity I can yield good estimates of the magnitude of the band bending V_S.[36,37] The optical and contactless attributes of PR make it useful for *in situ* studies in gaseous or liquid ambients.

This work used a small turbomolecularly pumped ultrahigh vacuum (UHV) chamber designed as described previously[38] with a base pressure of roughly 2×10^{-10} Torr. The optical cube chamber body was equipped with fused-silica optical ports, an inlet and handling system for O_2, ionization and thermocouple pressure gauges, and an electrical feedthrough for specimen support, heating, and temperature measurement.

Zn-terminated c-axis ZnO(0001) single crystals (CrysTec GmbH) of dimensions 1 cm $\times$ 1 cm $\times$ 0.05 cm were mounted by ultrahigh vacuum grade silver paint to a Ta backing plate that was heated resistively. Temperature was monitored with a type-K chromel–alumel thermocouple press-fit onto the edge of the ZnO. The sample was supplied in a vacuum bag, and exposed to air for less than 20 min before transfer into UHV. More importantly, *ex situ* XPS of samples with air exposure over many days showed only tiny traces of surface carbon, bonded mainly to nitrogen or alcohols. The surface roughness was measured *ex situ* by both scanning tunneling microscopy and atomic force microscopy to be <3 Å. Specimens were degreased by successive 5-min ultrasonic baths in electronic-grade acetone, isopropanol, and methanol, and where then mounted in the UHV chamber to minimize surface contamination. The chamber was then baked at 120°C for roughly 10 h to reach the base pressure. Experiments with oxygen used O_2 (S. J. Smith, $\geq$99.6% minimum, typical $\geq$99.995% with the balance being water ($<$1 ppm), or gases inert to ZnO) without further purification.

PR used methods closely related to those described elsewhere,[39] with some modest improvements to improve the signal-to-noise ratio. Specimens were pumped at near-normal incidence with a continuous-wave 10-mW diode laser operating at 355 nm. The beam diameter at the aperture was around 3 mm and projects a circular illuminated area on specimen with diameter around 5 mm. The transverse mode of pump beam is TEM_{00} with no defocused lens and the approximated average intensity is 0.051 W/cm^2. The scanning probe light was provided by a 75 W arc lamp directed through a monochromator of 0.25 m focal length operating at a spectral resolution of 6.4 nm. Directed at a 30° angle of incidence, the probe beam was shaped within the pump beam projected image on specimen surface through plano-convex lenses and then reflected into a photodiode that was carefully shielded from stray pump light. Phase-sensitive detection was accomplished with a mechanical chopper operating at 410 Hz in the pump beam together with conventional lock-in techniques. Scanning and data acquisition of R and ΔR were computer controlled. Spectra were collected at a stepping rate of 0.15 nm/s over the range 410–355 nm, coincident with the fundamental band edge of ZnO (E_g $\sim$303.07 kJ/mol [3.35 eV]).

Oxygen pressures P ranged from 5×10^{-9} to 760 Torr, with temperature varying between 300 and 346 K. The pressure range was limited by the capabilities of the vacuum chamber, and the temperature range was limited by room temperature at the low end (with no cooling capability) and the disappearance of the PR spectrum at $T >$380 K due to rapidly increasing thermionic emission of minority carriers that swamp the photocarriers. As P or T was varied in stages, signals for ΔR were monitored at a single wavelength corresponding to a peak in the PR spectrum. The full spectrum for determination of V_S was acquired only after ΔR had stabilized at its new (presumably equilibrium) value, generally within 2 h. The same spectra were obtained regardless of whether T or P was stepped up or down. Evidence for spurious photo-induced desorption as observed in other work[29] was sought by having probe beam positioning at a PR peak while instantly turn on the pump beam and monitor the peak signal change as a function of time, but no changes were found which rule out the occurrence of appreciable photo-induced desorption. This observation is probably due to the fact that our illumination intensity (0.051 W/cm^2) is much lower than the referenced work (1.9 W/cm^2), thus give us the capability to study the band bending change as a function of adsorption.

XPS was implemented in a standard configuration (Kratos Axis ULTRA, working pressure 5×10^{-9} Torr), with spectra collected both with and without low energy electron flooding (estimated energy near 1 eV) to check for possible artifacts connected with specimen charging. The X-ray energy was 1486.7 eV, monochromatized with a pass energy of 20 eV. As no fine structure in the valence band was required, but only the position of the valence band edge for determination of V_S, a standard 1486.7 eV X-ray source was used. Spectra were collected at four distinct positions on the specimen to check for spatial inhomogeneity; none was found. The XPS spectra were acquired in the presence of a remotely placed cold cathode ionization gauge. To confirm that optical illumination was unlikely to affect spectra, we did control experiments with and without illumination by a continuous UV laser (wavelength 355 nm, intensity 0.05 W/cm^2). No appreciable difference was observed in the resulting XPS spectra. The binding energy scale was calibrated using the Fermi level edge measured for an ion-bombarded gold sample. The energy distance between the Fermi level and conduction band edge was calculated based on a bulk carrier concentration (1×10^{12} cm^{-3}) reported in the literature[40] for ZnO specimens from the same manufacturer, growth history, and material specifications.

Results

Standard PR spectral analysis

Figure 1 shows a typical PR spectrum of ZnO(0001). The non-zero spectral amplitude manifests the existence of band bending. Qualitatively, the lineshape accords well with previous PR and eletroreflectance work on single-crystal ZnO.[41,42]

Quantitatively, the spectra were fitted by the three-point method developed by Aspnes and Rowe[43] to the standard third-derivative functional form given by Ref. 37

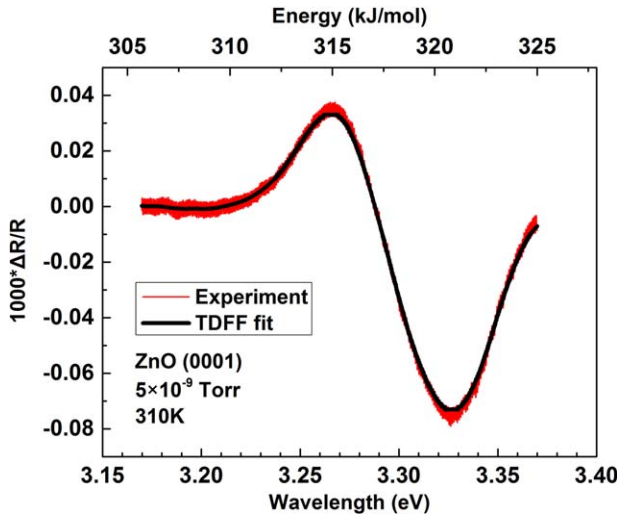

Figure 1. Typical PR spectra of Zn-rich ZnO(0001) at 310 K with theoretical line shape according to Eq. 1.

[Color figure can be viewed in the online issue, which is available at wileyonlinelibrary.com.]

$$\Delta R/R = Re[Ce^{i\varnothing}(E - E_{\text{crit}} + i\Gamma)^{-n}] \quad (1)$$

where C denotes an amplitude factor, ϕ a phase factor, Γ a broadening parameter, E_{crit} the energy of the critical point in the band structure, and n the associated dimension. The spectral structure in Figure 1 corresponds to a closely spaced pair of excitonic transitions (E_{0A} and E_{0B} in the notation of Ref. 41) that cannot be resolved at the temperatures of this work. Resolvable excitonic transitions normally correspond to $n = 2$. However, prior literature[41,42,44] has used $n = 2$, 2.5, or 3 to optimize the fit empirically, and $n = 3$ is the value used here for the unresolvable excitonic pair. The value of ϕ depends on the dielectric constant of the material and spatial variations of electric field with depth, and took a value between 1.09 and 1.13 that varied from spectrum to spectrum in this work with no particular pattern. Γ fluctuated slightly among specimens from 6.37 kJ/mol (66 meV) to 6.65 kJ/mol (69 meV) at 300 K, and increased linearly with T by 0.13 meV/K. This increase accords closely with the behavior of the broadening parameters for the individual E_{0A} and E_{0B} transitions.[41] E_{crit} varied with T between 320.95 kJ/mol (3.328 eV) and 319.31 kJ/mol (3.311 eV) according a standard Varshni's relation[45]

$$E_{\text{crit}}(T) = E_{\text{crit}}(0) - \frac{\alpha T^2}{T + \beta'} \quad (2)$$

with $E_{\text{crit}}(0) = 330.11$ kJ/mol (3.423eV), $\alpha = 0.072$ kJ/mol·K (0.75 meV/K), and $\beta' = 690$ K. These numbers agree closely with literature values, with $E_{\text{crit}}(0)$ well approximated by the average of the values for the individual E_{0A} and E_{0B} transitions. Figure 1 shows an example fit, which is quite good.

V_S was determined from the behavior of the amplitude factor C according to a method developed previously in this laboratory.[36] Briefly, C can be represented as

$$C = A_1 \ln\{A_2 I \exp(V_s/kT) + 1\} \quad (3)$$

where A_1 and A_2 describe optical properties of substrate, and k denotes Boltzmann's constant. Insertion of neutral density filters into the pump beam serves to vary I for a given value of T. The resulting plot of C vs. I can be fitted with A_1 and $A_2\exp(V_S/kT)$ as adjustable parameters. Figure 2 shows examples of such plots at several temperatures centered around 310 K, together with fits obtained by a standard nonlinear least squares technique. The consequent values of the parameter $A_2\exp(V_S/kT)$ can then be plotted in Arrhenius form to yield a value for V_S from the slope, as shown in Figure 3.

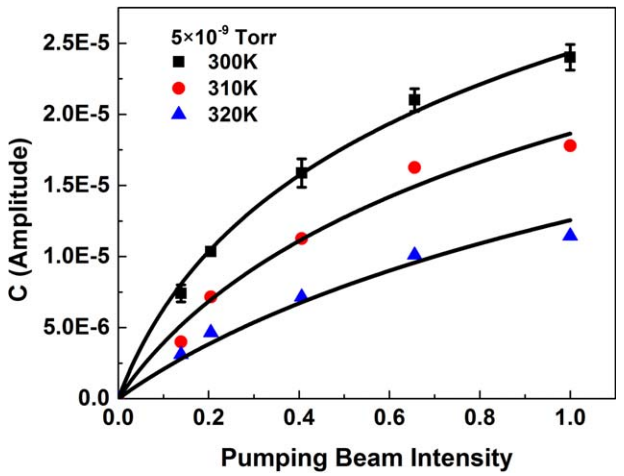

Figure 2. Variation of the PR amplitude factor *C* with illumination intensity for the spectra in Figure 1. Solid lines represent logarithmic fits according to Eq. 3.

[Color figure can be viewed in the online issue, which is available at wileyonlinelibrary.com.]

Development of method to extract temperature dependence of V_S

The data analysis procedure just outlined tacitly presupposes that V_S is independent of T, which was a good assumption in prior work with silicon.[36,37] With a temperature dependence of sufficient magnitude in V_S, Arrhenius plots such as that in Figure 3 should show curvature. In practice, however, such curvature would be difficult to discern even

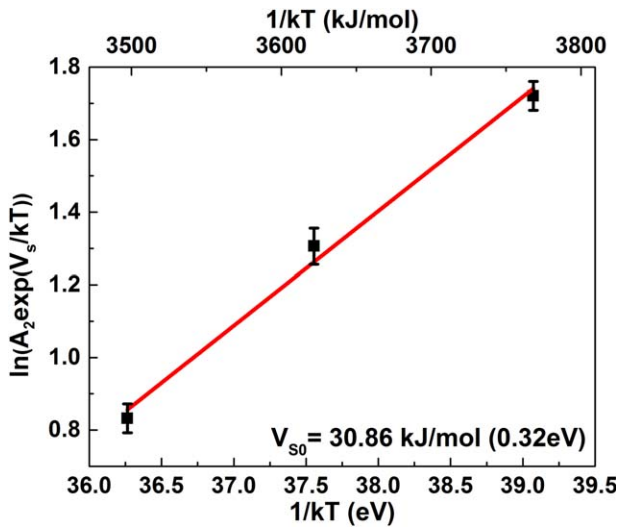

Figure 3. Arrhenius plot of the quantity $A_2\exp(Vs/kT)$ taken from the data of Figure 3. Slope of the plot gives V_{S0}.

[Color figure can be viewed in the online issue, which is available at wileyonlinelibrary.com.]

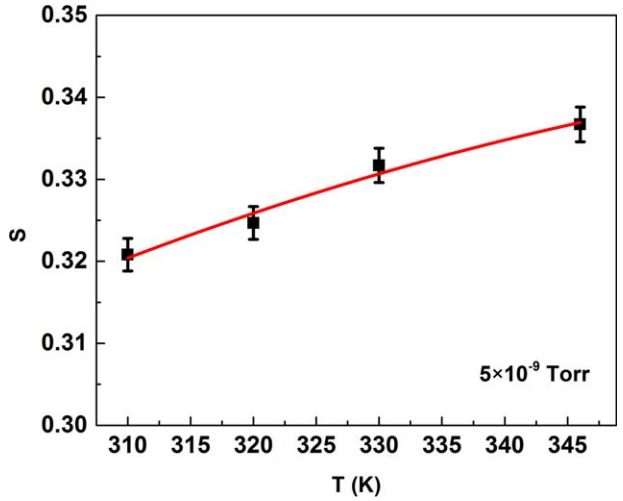

Figure 4. Variation of Arrhenius slope S as a function of temperature in oxygen pressure 5 × 10^{-9} Torr.

[Color figure can be viewed in the online issue, which is available at wileyonlinelibrary.com.]

with high-quality experimental data, and would require much more data for C vs. I at a given temperature. A more practical and accurate indication of temperature dependence in V_S comes from applying a new method over a range of target temperatures, each with C vs. I obtained over a modest range of T. Figure 4 shows the results of this latter approach. Each data point represents the center of a small temperature range extending ±10 K on either side. The entire temperature range of PR measurement encompassed 300–356 K—limited at the lower end by the inability of the apparatus to provide specimen cooling, and at the upper end by disappearance of the signal due to normal thermionic emission of minority carriers in the semiconductor.[36] Figure 4 shows that the nominal values of V_S rise steadily from 30.86 kJ/mol (0.32 eV) to nearly 32.79 kJ/mol (0.34 eV). This increase lies well outside the error bars of the measurement, which points to the need for an adaptation of the method. As shown below, such an adaptation is possible, but requires some additional data about V_S from an experimental technique in addition to PR.

Application of the chain rule to Eq. 3 shows that the slope (S) of an Arrhenius plot of $A_2\exp(V_S/kT)$ equals $V_S - TdV_S/dT$. The derivative dV_S/dT obviously vanishes when V_S remains constant. However, in cases where dV_S/dT does not vanish, the PR spectra yield values for Vs that are inaccurate. To see why this is so, consider an arbitrary function form $V_S(T)$. As long as V_S and dV_S/dT are a continuous functions of T (excluding discontinuities in V_S due to first-order surface phase transitions, e.g.), $V_S(T)$ can be linearized over a narrow range of T by Taylor series expansion into the form

$$V_S = V_{S0} + \beta T \tag{3a}$$

where V_{S0} and β are constants. An Arrhenius plot of $A_2\exp(V_S/kT)$ yields

$$S = d/d(1/kT)\{A_2\exp(V_S/kT))\} = V_S - TdV_S/dT = V_{S0} \tag{3b}$$

In other words, the constant β cannot be independently determined from the PR data. An additional measurement of V_S by an experimental technique other than PR is required to establish the value of β.

The correction provided by the βT term is nontrivial, as can be seen from the following example. A crude estimate of β may be drawn from the T dependence in V_S suggested by the slope in Figure 3: that is, $\beta \approx$ (32.79 – 30.86 kJ/mol)/(345–310 K) = 54.97 J/mol·K (0.57 meV/K). At 310 K, this value of β would translate into $V_S = V_{S0} + \beta T$ = 30.86 + 17.36 = 48.219 kJ/mol (0.50 eV), or a correction of over 50% in the base value of V_S.

To determine β more accurately, we measured an anchor value of V_S by XPS at 310 K as detailed below. The pressure was of 5 × 10^{-9} Torr lay at one end of the range of pressures examined with PR. The XPS yielded V_S = 74.26 kJ/mol (0.77 eV), which leads to values for V_{S0} and β of 31.63 kJ/mol (0.328 eV) and 0.135 kJ/mol·K (1.4 meV/K), respectively.

Figure 5 shows XPS spectra used to determine the energy E_v of the valance band maximum at the surface, referenced to the Fermi energy E_f. A linear fit to the low-binding-energy portion of the ZnO spectrum was extrapolated linearly to the baseline, with the intersection occurring at 415.66 kJ/mol (4.31 eV). The instrument was calibrated in a similar way to determine the binding energy corresponding to E_f (uniform among materials) through an analogous spectrum of gold (shown inset in Figure 5), the position of whose Fermi level is readily reproduced among instruments. This binding energy was 55.94 kJ/mol (0.58 eV).

The position of E_f relative to the conduction band minimum E_c was calculated based on the concentration n of majority carriers (free electrons in the conduction band) via the following relation

$$E_c - E_f = kT\ln\left(\frac{N_c}{n}\right) \tag{4}$$

where, k is Boltzmann's constant, and $n = 1 \times 10^{12}$ cm^{-3} given by Ref. 40. N_c denotes the effective density of conduction band states given by

$$N_c = 2\left(\frac{2\pi m_e^* kT}{h}\right)^{\frac{3}{2}} \tag{5}$$

where $m_e^* = 0.27\ m_e$[46] is the effective electron mass of ZnO, with the actual electron mass being m_e. This calculation leads

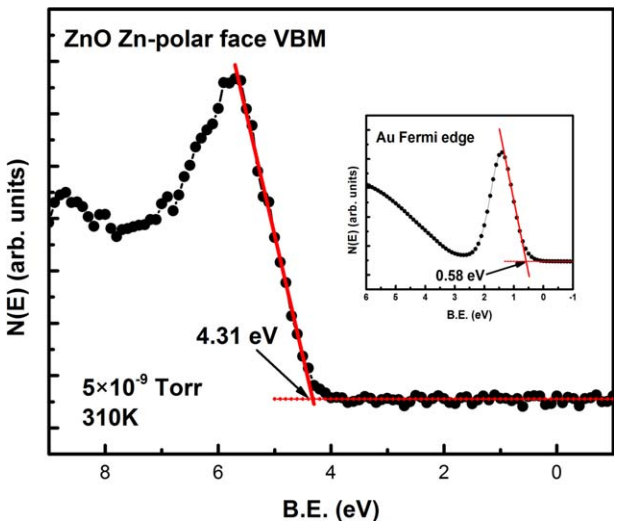

Figure 5. Linear fits to the leading edge of the valence band XPS spectra from ZnO Zn-polar face, and Ion bombarded gold reference sample (inset) at 5 × 10^{-9} Torr, 310 K.

[Color figure can be viewed in the online issue, which is available at wileyonlinelibrary.com.]

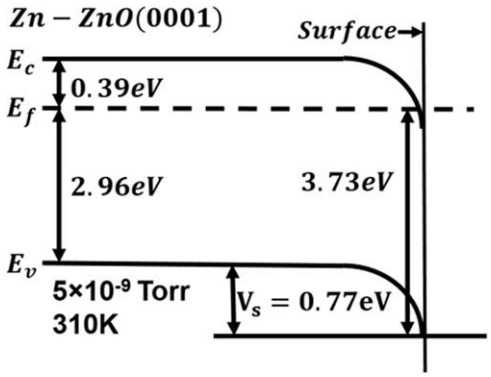

Figure 6. Band structure of Zn-rich ZnO(0001) at 5 × 10^{-9} Torr, 310 K. The bands bend downward by 0.77 eV at the free surface edge.

to $E_c - E_f = 37.61$ kJ/mol (0.39 eV). The schematic energy band diagram of Figure 6 shows how this number is used with the room-temperature band gap energy E_g of 323.07 kJ/mol (3.35 eV) to determine the position of E_v in the deep bulk, leading to $E_f - E_c = 323.07 - 35.68$ kJ/mol = 285.46 kJ/mol(3.35 − 0.39 eV = 2.96 eV). The corresponding energy difference $(E_f - E_v)_{surf}$ at the surface equals the difference in binding energy measured for the Fermi energy and valence band maximum, that is, 415.66 − 55.94 = 359.72 kJ/mol (4.31 − 0.58 = 3.73 eV). Finally, the difference between E_v at the surface and in the bulk equals 359.72 − 285.46 = 74.26 kJ/mol (3.73 − 2.96 = 0.77 eV), which represents the magnitude of V_S. The bands are bent downward, signifying the formation of an accumulation region of majority carriers near the surface. Indeed, the magnitude of the band bending is so large that E_f resides within the conduction band at the surface, putting the near-surface region into a degenerate condition with metal-like electrical conductivity. The identity of bulk ZnO as a transparent conductive oxide in response to heavy doping is well known,[47] and the present results simply confirm that behavior in response to band bending.

T and P dependence of V_S

Figure 7 shows the values of V_S obtained as a function of T at $P = 5 \times 10^{-9}$ Torr. V_S varies between 74.26 kJ/mol (0.77 eV) and 79.08 kJ/mol (0.82 eV). The function form is linear, which is consistent with the assumption embodied in Eq. 3a. As the temperature range in Figure 7 is notably wider than the ranges used for computing V_S at each point, the local linearity assumption of Eq. 3a would not necessarily propagate through into a straight line in Figure 7.

The analytical method described here tacitly assumes that V_S and C are linearly related, an assumption that has been justified elsewhere.[38] Thus, if V_S has been measured by this method at a given value of T, it is not necessary to replicate the entire intensity-dependent set of experiments when changing P at the same T. It is necessary to obtain C at only one value of I. In other words, spectra can be measured one after another as P is varied. Even better, as lineshape depends only on T and not on P, only the value of $\Delta R/R$ at one wavelength is required, as Eq. 1 implies that value will be proportional to C. Typically this wavelength should be chosen at a spectral extremum (e.g., near 321.15 kJ/mol (3.33 eV) in Figure 1) to maximize the signal-to-noise ratio and minimize instrumental drift effects.

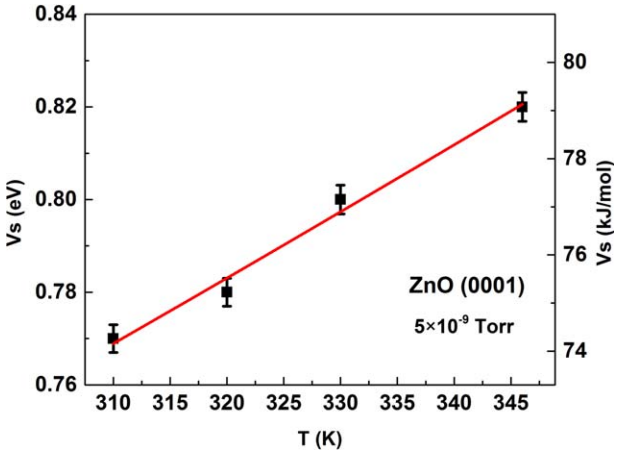

Figure 7. Variation of surface potential *Vs* as a function of temperature in oxygen pressure 5 × 10^{-9} Torr.

[Color figure can be viewed in the online issue, which is available at wileyonlinelibrary.com.]

Figure 8 shows V_S at 310 K over oxygen pressures ranging from 5×10^{-9} Torr to atmospheric. V_S decreases from 74.26 kJ/mol (0.77 eV) down to nearly 54.01 kJ/mol (0.56 eV) over that range, with a nonlinear functional form. If both T and P are allowed to vary, V_S exhibits a maximum of 79.08 kJ/mol (0.82 eV) at 346 K and 5×10^{-9} Torr, and a minimum of 54.97 kJ/mol (0.57eV) at 310 K and 760 Torr. Thus, varying a combination of T and P enables a variation of V_S by a total of 24.11 kJ/mol (0.25 eV) in this range of temperatures and pressures.

Discussion

Development of a surface potential at a semiconductor surface has been well reviewed in the literature[48,49] and results from charge exchange between the bulk and surface due to the existence of donor or acceptor energy states associated with dangling bonds, surface reconstructions, surface defects, or adsorbates. For polar ZnO surfaces, numerous atomic reconstructions exist whose stability depends on T and P.[50] The available literature for Zn-terminated ZnO(0001) is divided about the magnitude of Vs

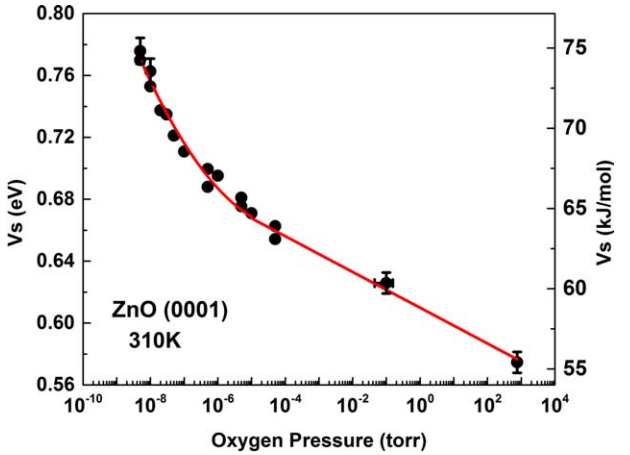

Figure 8. Variation of band bending *Vs* with oxygen pressure at sample temperature 310 K.

[Color figure can be viewed in the online issue, which is available at wileyonlinelibrary.com.]

for this surface under high vacuum conditions near room temperature, but there is uniform agreement that an accumulation region forms in response to downward band bending. Ultraviolet photoelectron spectroscopy (UPS) and electron energy loss spectroscopy have placed V_S at 19.29–28.93 kJ/mol (0.2–0.3 eV).[51,52] Other UPS work has placed V_S at 86.80 kJ/mol (0.9 eV) for the clean surface.[53] Exposure of the surface to a remote O_2 plasma (20% O_2/80% He) changed V_S to 28.93 kJ/mol (0.3eV) upward (i.e., depletion).[53] However, unless unusual care was taken to avoid exposure of the surface to stray ions, a certain degree of ion bombardment would have been possible. Surface and subsurface defect formation due to the bombardment could have created a significant concentration of acceptor defects that would bend the bands upward. More recently, using synchrotron based XPS, Heinhold et al. found band bending at room temperature on Zn-terminated ZnO(0001) is downward by 57.86 kJ/mol (0.6 eV).[54] Thus, the present value of $V_S \approx 77.15$ kJ/mol (0.8 eV) lies well within the range of previous work.

T and P dependence

The magnitude of V_S is substantially larger than that suggested based on PR alone, either taken directly from Figure 3 or computed indirectly by estimating dV_S/dT from Figure 4. The actual value of $\beta = dV_S/dT$ is more than a factor of two larger than the estimate suggested by Figure 4. These differences emphasize the importance of incorporating the temperature dependence of V_S explicitly into the computation of V_S itself, as well as the need for an independent experimental anchor point for the PR data. Note also that PR cannot measure the direction of the band bending (or equivalently, the sign of V_S), but only the magnitude of V_S.

The closest available literature report concerning the T dependence of V_S on Zn-terminated ZnO(0001) was performed in UHV and reported a downward band bending with slowly declining magnitude from 57.86 kJ/mol (0.6 eV) at room temperature to 43.40 kJ/mol (0.45 eV) at 650°C.[54] However, the magnitude of V_S then decreased more sharply by roughly 38.576 kJ/mol (0.4 eV) to 19.29 kJ/mol (0.2 eV) as T increased further to 750°C. The authors attributed such a large change over such a small range of temperature to an unspecified surface reorganization. However, they noted that Zn-terminated ZnO(0001) supports appreciable concentrations of adsorbed OH and H_2O on loading into UHV at room temperature, The adsorbed H_2O disappears on heating to 750°C, but some OH always remains (although at slowly decreasing concentrations). The results shown in this work encompass a much narrower range of temperatures. Yet, the magnitude of V_S increases (0.134 kJ/mol·K [1.4 meV/K]), rather than decreases. The detailed results of Ref. 54 suggest that the concentration of adsorbed OH should remain constant in this temperature range.

Moreover, the change in V_S observed here is smooth and continuous, which would not be expected for a first-order phase transition between surface reconstructions. The more gradual evolution of V_S more likely represents a change in adsorption state, as adsorbed oxygen was present in equilibrium. The change in V_S would then reflect the behavior of the adsorption isotherm. Indeed, the highest values of V_S correspond to the highest temperatures and lowest oxygen pressures—both of which tend to decrease the concentration of adsorbate in a typical isotherm.

The influence of gas adsorption on V_S of semiconductors has been known for many decades. In the case of oxygen, for example, photoemission spectroscopy has demonstrated substantial changes in V_S for both Si and III–V semiconductors,[55–58] and PR has confirmed similar effects.[37,59] Less work exists for metal oxide substrates, but there still exists a useful literature for comparison—including for ZnO.[53,54,60,61] For example, Chevtchenko et al.[60] usedscanning Kelvin probe microscopy to observe upward band banding for Zn-terminated ZnO(0001) in the range 2.89–38.58 kJ/mol (0.03–0.40 eV), attributed to adsorption of OH from the ambient atmospheric background containing water. Heinhold et al.[54] used XPS for the same surface intentionally dosed with water. For surfaces already annealed to 750°C, room-temperature exposure to even large amounts of water (10^4 L) did not change V_S, but pumping away the background after dosing did increase the magnitude of V_S by 9.64 kJ/mol (0.1 eV). Subsequent room-temperature dosing with up to 103 L of H2 decreased V_S by 19.29 kJ/mol (0.2 eV). Coppa et al.[53] used a remote oxygen plasma as described above to induce substantial changes in V_S. The authors attributed the effects to the adsorption of undefined "oxygen species," but as indicated above, the results could have been complicated by ion bombardment effects. Indeed, early quantum computations suggested that atomic oxygen should not adsorb on Zn-terminated ZnO(0001),[61] appearing to confirm experimental literature[62] suggesting neither atomic nor molecular oxygen should bond strongly. By contrast, recent computational literature[63] reports that both species should adsorb strongly (190–290 kJ/mol [2–3eV/adsorbate]), which is consistent with this work.

This work shows that molecular oxygen decreases V_S on Zn-terminated ZnO(0001) by a substantial amount—up to roughly 19.29 kJ/mol (0.2 eV). Note that ZnO the downward band bending on the clean surface represents a response to donor-like surface states. It has been proposed elsewhere for other ZnO surfaces that O_2, an electron scavenger, decreases the band bending by extracting electrons from the surface through adsorption,[64,65] thereby becoming chemically adsorbed O_2^-.[53,66–68] This effect would keep electrons localized near the surface instead of being donated to the conduction band and rendering the surface more positively charged.

Implications for defect engineering

Recent isotopic self-diffusion measurements of O in TiO_2[20] and ZnO (Manipulation of point defects within metal oxide semiconductors via surface polarity, in preparation) have shown that near-surface electric fields can induce accumulation of injected point defects within the space charge region. Although diffusion induces the injected interstitial atoms to spread into the underlying bulk, appropriate combinations of electric field direction and defect charge can attract the injected defects back toward the surface. In other words, electric drift can retard the diffusional migration of the charged defects through the space charge layer, resulting in a longer residence time within that layer. The extended residence time causes the defects to pile up, with the effect scaling quadratically with V_S.[61] In the present case, the variation of V_S between 54.97 kJ/mol (0.57 eV) and 79.08 kJ/mol (0.82 eV) would translate into an enhanced O interstitial concentration by a factor of about three. Related transport modeling[61] has shown that depletion of such defects can occur as well depending on the sign of charge on the defects and the direction of the electric field. The magnitude of V_S required for such effects can be quite small—on the order of a few meV.

Other mechanisms for defect pile up in the space charge region have also been identified due to charging contributions to the O vacancy formation energy (for Fe-doped $SrTiO_3(100)$[69]) or to changes in the charge state of the defect (for boron near Si/SiO_2 interfaces[70,71]). In the latter case involving ion implantation, the surface serves as a net sink for point defects by annihilation rather than a net source by injection. Regardless of the specific physical mechanism, however, or whether the surface is used as a source or sink, the ability of V_S to serve as a tool to influence the spatial distribution of defects is clear.

Under suitable conditions, V_S can be used as a tool to control the net rate of defect injection or annihilation at the surface as well. The ability of surface electric fields to inhibit the migration rate of interstitial atoms toward the surface in a controlled way is already well established in Si.[72] The field-based attraction of injected interstitials toward the surface described in Ref. 65 can become large enough to affect not only the defects' spatial distribution (when V_S is in the meV range), but also the net injection rate deeper into the bulk (when Vs is considerably larger).

Adsorption of simple gases affects V_S on metal oxide semiconductors other than ZnO. For example, Göpel et al. have shown that adsorption of O_2, H_2, CO, and CO_2 can affect V_S on TiO_2.[73] Thus, we surmise that use of T and P to control V_S via the isotherm and thereby accomplish defect engineering may generalize to other metal oxide surfaces as well. The properties of the isotherm (as embodied in the enthalpy and entropy for adsorption) would need to be matched to the temperature range required for defect mobility. The present case of O_2 on ZnO(0001) near room temperature may not be well matched, for example, to a defect engineering process of injecting O interstitials to annihilate O vacancies 100 μm deep—requiring temperatures several hundred degrees higher.

In liquids, control of V_S can be accomplished electrochemically via suitably applied potentials. Indeed, such a phenomenon seems to underlie the defect manipulation that seems to account for the recent report[74] of enhanced room-temperature oxygen storage by TiO_2 nanotubes by electrochemical means.

The method described here for using adsorption P and T to control V_S for defect engineering is distinct from, but complementary to, another adsorption-based mechanism for controlling defect behavior. This other mechanism involves controlled saturation of surface dangling bonds, and has been demonstrated for sulfur on TiO_2[30] and nitrogen on Si.[17] In both cases, defect injection and/or annihilation rates were varied by 1-2 orders of magnitude through adsorption of submonolayer concentrations of the controlling element—to the extent that the majority species responsible for carrying self-diffusional flux actually changed. In this mechanism the controlled saturation of dangling bonds at the surface modulates the ease with which point defects can exchange with the surface. In principle, the two methods may be combined and coordinated to facilitate defect engineering through the surface.

Conclusion

This work has extended the *in situ* optical technique of PR, augmented by a new data analysis method and XPS, to demonstrate how isotherms for gaseous adsorption may be used to control V_S for Zn-terminated polar ZnO(0001) via temperature and gaseous oxygen pressure. At the modest temperatures of this work, such information by itself could be useful to interpret and control the operation of gas sensors. An equivalent concept used at much higher temperatures characteristic of device processing could be used, together with computational tools for modeling the transport-reaction network, to accomplish defect engineering via a combination of surface mechanisms involving V_S and controlled saturation of surface dangling bonds. The approach will likely yield results that depend on crystallographic orientation—a variable yet to be explored.

Acknowledgments

This work was supported by NSF (DMR 13-06822). Ming Li gratefully acknowledges fellowship support from the Dow Chemical Company. The authors also acknowledge the help from Dr. Rick Haasch for assisting XPS measurement and data interpretation.

Literature Cited

1. Fahey PM, Griffin PB, Plummer JD. Point defects and dopant diffusion in silicon. *Rev Mod Phys*. 1989;61:289.
2. Fergus JW. Doping and defect association in oxides for use in oxygen sensors. *J Mater Sci*. 2003;38:4259–4270.
3. Comini E. Metal oxide nano-crystals for gas sensing. *Anal Chim Acta*. 2006;568:28–40.
4. Yamazoe N. New approaches for improving semiconductor gas sensors. *Sen Actuators B Chem*. 1991;5:7–19.
5. Wang B, Jing L, Qu Y, Li S, Jiang B, Yang L, Xin B, Fu H. Enhancement of the photocatalytic activity of TiO_2 nanoparticles by surface-capping DBS groups. *Appl Surf Sci*. 2006;252:2817–2825.
6. Zhang Y, Kolmakov A, Chretien S, Metiu H, Moskovits M. Control of catalytic reactions at the surface of a metal oxide nanowire by manipulating electron density inside it. *Nano Lett*. 2004;4:403–407.
7. Chua YPG, Gunasooriya GTKK, Saeys M, Seebauer EG. Controlling the CO oxidation rate over Pt/TiO2 catalysts by defect engineering of the TiO_2 support. *J Catal*. 2014;311:306–313.
8. Ong SWD, Lin J, Seebauer EG. Control of methylene blue photooxidation rate over polycrystalline anatase TiO_2 thin films via carrier concentration. *J Phys Chem C*. 2015;119:11662–11671.
9. Chow WW, Koch SW. *Semiconductor-Laser Fundamentals: Physics of the Gain Materials*. Berlin Heidelberg: Springer, Springer Science & Business Media, 2013.
10. Guha S, DePuydt JM, Haase MA, Qiu J, Cheng H. Degradation of II-VI based blue-green light emitters. *Appl Phys Lett*. 1993;63:3107–3109.
11. Lutz G. *Semiconductor Radiation Detectors, Vol. 10*. Berlin: Springer, 1999.
12. Kurtz SR, Allerman AA, Jones ED, Gee JM, Banas JJ, Hammons BE. InGaAsN solar cells with 1.0 eV band gap, lattice matched to GaAs. *Appl Phys Lett*. 1999;74:74–76.
13. Yoshio N, Doering R. *Handbook of Semiconductor Manufacturing Technology*. Boca Raton, Florida: CRC Press, 2000.
14. Siffert P, Krimmel E. *Silicon: Evolution and Future of a Technology*. Berlin Heidelberg: Springer Science & Business Media, 2013.
15. Jones EC, Ishida E. Shallow junction doping technologies for ULSI. *Mater Sci Eng: R: Rep*. 1998;24:1–80.
16. Colombeau B, Yeong SH, Tan DXM, Smith AJ, Gwilliam RM, Ng CM, Mok KRC, Benistant F, Chan L. Ultra-Shallow Junction Formation—Physics and Advanced Technology. In: *Proceedings of the 17th International Conference on Ion Implantation Technology*, *AIP*, Monterey, CA, 2008:11–18.
17. Gossmann HL. Junction formation and its device impact through the nodes: from single to coimplants, from beam line to plasma, from single ions to clusters, and from rapid thermal annealing to laser thermal processing. *J Vac Sci Technol B*. 2008;26:267–272.
18. Seebauer EG, Noh KW. Trends in semiconductor defect engineering at the nanoscale. *Mater Sci Eng: R: Rep*. 2010;70:151–168.
19. Kucheyev SO, Williams JS, Jagadish C. Ion-beam-defect processes in group-III nitrides and ZnO. *Vacuum*. 2004;73:93–104.
20. Ronning C, Carlson EP, Davis RF. Ion implantation into gallium nitride. *Phys Rep*. 2001;351:349–385.
21. Wesch W. Ion implantation in III–V compounds. *Nucl Instrum Methods Phys Res B*. 1992;68:342–354.
22. Anpo M, Dohshi S, Kitano M, Hu Y, Takeuchi M, Matsuoka M. The preparation and characterization of highly efficient titanium oxide-based photofunctional materials. *Annu Rev Mater Res*. 2005;35:1–27.
23. Ni M, Leung MKH, Leung DYC, Sumathy K. A review and recent developments in photocatalytic water-splitting using TiO_2 for hydrogen production. *Renew Sustain Energy Rev*. 2007;11:401–425.

24. Nowotny MK, Sheppard LR, Bak T, Nowotny J. Defect chemistry of titanium dioxide. Application of defect engineering in processing of TiO_2-based photocatalysts. *J Phys Chem C*. 2008;112:5275–5300.
25. Walle V, Chris G. Defect analysis and engineering in ZnO. *Physica B Condens Matter*. 2001;308:899–903.
26. Current MI, Inoue M, Nakashima S, Ohno S, Kuribara M, Matsunaga Y, Hara T. Defect engineering of p+-junctions by multiple-species ion implantation. *Nucl Instrum Methods Phys Res B*. 1993;74:175–180.
27. Vaidyanathan R, Felch S, Graoui H, Foad MA, Kondratenko Y, Seebauer EG. Nonthermal illumination effects on ultra-shallow junction formation. *Appl Phys Lett*. 2011;98:194104.
28. Kondratenko Y, Seebauer EG. Interface-mediated photostimulation effects on diffusion and activation of boron implanted into silicon. *ECS J Solid State Sci Technol*. 2013;2:235–242.
29. Seebauer EG, Dev K, Jung MYL, Vaidyanathan R, Kwok CTM, Ager JW, Haller EE, Braatz RD. Control of defect concentrations within a semiconductor through adsorption. *Phys Rev Lett*. 2006;97:055503.
30. Hollister AG, Gorai P, Seebauer EG. Surface-based manipulation of point defects in rutile TiO2. *Appl Phys Lett*. 2013;102:231601.
31. Gorai P, Seebauer EG. Kinetic model for electric-field induced point defect redistribution near semiconductor surfaces. *Appl Phys Lett*. 2014;105:021604.
32. Pangan-Okimoto KM, Gorai P, Hollister AG, Seebauer EG. Model for oxygen interstitial injection from the rutile Tio_2 (110) surface into the bulk. *J Phys Chem C*. 2015;119:9955–9965.
33. Klein A, Körber C, Wachau A, Säuberlich F, Gassenbauer Y, Harvey SP, Proffit DE, Mason TO. Transparent conducting oxides for photovoltaics: manipulation of Fermi level, work function and energy band alignment. *Materials*. 2010;3:4892–4914.
34. Djurišić AB, Choy WCH, Roy WAL, Leung YH, Kwong CY, Cheah KW, Rao TKG, Chan WK, Lui HF, Surya C. Photoluminescence and electron paramagnetic resonance of ZnO tetrapod structures. *Adv Funct Mater*. 2004;14:856–864.
35. Lin B, Fu Z, Jia Y. Green luminescent center in undoped zinc oxide films deposited on silicon substrates. *Appl Phys Lett*. 2001;79:943–945.
36. Ditchfield R, Llera-Rodriguez D, Seebauer EG. Semiconductor surface diffusion: nonthermal effects of photon illumination. *Phys Rev B*. 2000;61:13710.
37. Dev K, Seebauer EG. Band bending at the Si (111)–SiO_2 interface induced by low-energy ion bombardment. *Surf Sci*. 2004;550:185–191.
38. Carlson CR, Buechter WF, Che-Ibrahim F, Seebauer EG. Adsorption/desorption kinetics of H2O on GaAs (100) measured by photoreflectance. *J Chem Phys*. 1993;99:7190–7197.
39. Sellers MCK, Seebauer EG. Investigation of nanostructured TiO_2 surface and interface electric fields with photoreflectance spectroscopy. *AIChE J*. 2013;59:1049–1055.
40. Nickel NH, Terukov E. Zinc oxide-a material for micro-and optoelectronic applications. In: *Proceedings of the Nato Advanced Research Workshop on Zinc Oxide as a Material for Micro-and Optoelectronic Applications*, held in St. Petersburg, Russia, from 23 to 25 June 2004: Berlin Heidelberg: Springer Science & Business Media, 2006:194: 194–197.
41. Ozaki S, Mishima T, Adachi S. Photoreflectance spectroscopy of ZnO for ordinary and extraordinary rays. *Jpn J Appl Phys*. 2003;42:5465.
42. Tseng AH, Chiang YF, Wang DP. Determination of transition mechanism and polarity of a c-plane zno bulk by using contactless electroreflectance spectrum. *Key Eng Mater*. 2013;538:189–192.
43. Aspnes DE, Rowe JE. Resonant nonlinear optical susceptibility: electroreflectance in the low-field limit. *Phys Rev B*. 1972;5:4022.
44. Kudrawiec R, Misiewicz J, Guziewicz E, Godlewski M. Contactless electroreflectance of ZnO layers grown by atomic layer deposition at low temperature. *Semicond Sci Technol*. 2011;26:075012.
45. Varshni YP. Temperature dependence of the energy gap in semiconductors. *Physica*. 1967;34:149–154.
46. Han J, Mantas PQ, Senos AMR. Defect chemistry and electrical characteristics of undoped and Mn-doped ZnO. *J Eur Ceram Soc*. 2002;22:49–59.
47. Ellmer K, Klein A, Rech B. *Transparent Conductive Zinc Oxide: Basics and Applications in Thin Film Solar Cells*. Berlin Heidelberg: Springer Science & Business Media, 2007:104.
48. Zhang Z, Yates JT Jr,. Band bending in semiconductors: chemical and physical consequences at surfaces and interfaces. *Chem Rev*. 2012;112:5520–5551.
49. Mönch W. *Electronic Properties of Semiconductor Interfaces*. Springer Science & Business Media, 2004:43.
50. Dulub O, Diebold U, Kresse G. Novel stabilization mechanism on polar surfaces: ZnO (0001)-Zn. *Phys Rev Lett*. 2003;90:016102.
51. Lagowski J, Sproles ES Jr, Gatos HC. Quantitative study of the charge transfer in chemisorption; oxygen chemisorption on ZnO. *J Appl Phys*. 1977;48:3566–3575.
52. Jacobi K, Zwicker G, Gutmann A. Work function, electron affinity and band bending of zinc oxide surfaces. *Surf Sci*. 1984;141:109–125.
53. Coppa BJ, Fulton CC, Kiesel SM, Davis RF, Pandarinath C, Burnette JE, Nemanich RJ, Smith DJ. Structural, microstructural, and electrical properties of gold films and Schottky contacts on remote plasma-cleaned, n-type ZnO {0001} surfaces. *J Appl Phys*. 2005;97:103517.
54. Heinhold R, Williams GT, Cooil SP, Evans DA, Allen MW. Influence of polarity and hydroxyl termination on the band bending at ZnO surfaces. *Phys Rev B*. 2013;88:235315.
55. Gudat W, Eastman DE. Electronic surface properties of III–V semiconductors: excitonic effects, band-bending effects, and interactions with Au and O adsorbate layers. *J Vac Sci Technol*. 1976;13:831–837.
56. Stiles K, Mao D, Kahn A. Oxygen adsorbed on GaAs (110) surfaces: the effect of temperature on band bending. *J Vac Sci Technol B*. 1998;6:1170-1173.
57. Winer K. Band bending and oxygen-induced defects in a-Si: H. *J Vac Sci Technol B*. 1989;7:1226–1231.
58. Engstrom JR, Bonser DJ, Engel T. The reaction of atomic oxygen with Si (100) and Si (111): II. Adsorption, passive oxidation and the effect of coincident ion bombardment. *Surf Sci*. 1992;268:238–264.
59. Seebauer EG. Oxidation and annealing of GaAs (100) studied by photoreflectance. *J Appl Phys*. 1989;66:4963–4972.
60. Chevtchenko SA, Moore JC, Özgür Ü, Gu X, Baski AA, Morkoc H, Nemeth B, Nause JE. Comparative study of the (0001) and (0001xAF) surfaces of ZnO. *Appl Phys Lett*. 2006;89:2111.
61. Allen VM, Jones WE, Pacey PD. The interaction of oxygen and carbon monoxide with iron oxide, nickel oxide and zinc oxide surfaces: a molecular orbital study. *Surf Sci*. 1989;220:193–205.
62. Dorn R, Lüth H. The adsorption of oxygen and carbon monoxide on cleaved polar and nonpolar ZnO surfaces studied by electron energy loss spectroscopy. *Surf Sci*. 1977;68:385–391.
63. Warschkow O, Chuasiripattana K, Lyle MJ, Delley B, Stampfl C. Cu/ZnO (0001) under oxidating and reducing conditions: a first-principles survey of surface structures. *Phys Rev B*. 2011;84:125311.
64. Ozawa K, Mase K. Comparison of the surface electronic structures of H-adsorbed ZnO surfaces: an angle-resolved photoelectron spectroscopy study. *Phys Rev B*. 2011;83:125406.
65. Allen MW, Swartz CH, Myers TH, Veal TD, McConville CF, Durbin SM. Bulk transport measurements in ZnO: the effect of surface electron layers. *Phys Rev B*. 2010;81:075211.
66. Iwamoto M, Yoda Y, Yamazoe N, Seiyama T. Study of metal oxide catalysts by temperature programmed desorption. 4. Oxygen adsorption on various metal oxides. *J Phys Chem*. 1978;82:2564–2570.
67. Kushwaha A, Aslam M. Defect induced high photocurrent in solution grown vertically aligned ZnO nanowire array films. *J Appl Phys*. 2012;112:054316.
68. Tench AJ, Lawson T. Oxygen species adsorbed on zinc oxide. *Chem Phys Lett*. 1971;8:177–178.
69. De S, Roger A, Martin M. Using $^{18}O/^{16}O$ exchange to probe an equilibrium space-charge layer at the surface of a crystalline oxide: method and application. *Phys Chem Chem Phys*. 2008;10:2356–2367.
70. Jung MYL, Gunawan R, Braatz RD, Seebauer EG. Effect of near-surface band bending on dopant profiles in ion-implanted silicon. *J Appl Phys*. 2004;95:1134–1140.
71. Gorai P, Kondratenko YV, Seebauer EG. Mechanism and kinetics of near-surface dopant pile-up during post-implant annealing. *J Appl Phys*. 2012;111:094510.
72. Dev K, Jung MYL, Gunawan R, Braatz RD, Seebauer EG. Mechanism for coupling between properties of interfaces and bulk semiconductors. *Phys Rev B*. 2003;68:195311.
73. Göpel W, Rocker G, Feierabend R. Intrinsic defects of TiO_2(110): interaction with chemisorbed O_2, H_2, CO, and CO_2. *Phys Rev B*. 1983;28:3427.
74. Close T, Tulsyan G, Diaz CA, Weinstein SJ, Richter C. Reversible oxygen scavenging at room temperature using electrochemically reduced titanium oxide nanotubes. *Nature Nanotechnol*. 2015;10:418–422.

Manuscript received June 19, 2015, and revision received Aug. 25, 2015.